FEATURE ARTICLE

Optical Nonlinearities and Ultrafast Carrier Dynamics in Semiconductor Nanocrystals

Victor I. Klimov†

Chemical Science and Technology Division, CST-6, MS-J585, Los Alamos National Laboratory, Los Alamos, New Mexico 87545

Received: December 16, 1999; In Final Form: March 15, 2000

Femtosecond transient absorption in the visible and infrared spectral ranges has been applied to study carrier dynamics and mechanisms for resonant optical nonlinearities in CdSe nanocrystals (NCs) with a variety of surface passivations. Sequential filling of the 1S, 1P, and 1D atomic-like electron orbitals, governed by Fermi statistics, is clearly observed in the NC bleaching spectra recorded at progressively higher pump intensities. We observe that electron−hole (e−h) spatial separation strongly affects electron intraband dynamics. Such dependence indicates a nonphonon energy relaxation mechanism involving e−h interactions. A strong difference in electron and hole relaxation behavior in the stage following initial intraband relaxation is observed. In contrast to electron relaxation, which is sensitive to the quality of surface passivation (i.e., is affected by trapping at surface defects), depopulation dynamics of the initially-excited hole states are identical in NCs with different surface properties, suggesting that these dynamics are due to relaxation into intrinsic NC states. In the regime of multiparticle excitation, a quantization of relaxation rates corresponding to different multiple e−h pair states is observed. This effect is explained in terms of quantum-confined Auger recombination.

1. Introduction

Semiconductor nanocrystals (NCs) or quantum dots (QDs) represent a class of quasi-zero-dimensional objects in which carrier motion is restricted in all three directions. Bulk crystalline structure is preserved in NCs; however, due to three-dimensional (3D) quantum confinement NCs have atomic-like discrete energy spectra that are strongly size dependent.[1−4]

Chemical synthesis allows fabrication of NCs in the size range from 1 to 10 nm. Synthetic methods are particularly well developed for II−VI NCs. The two main chemical routes for preparation of these NCs are high-temperature precipitation in molten glasses[5,6] and colloidal synthesis using, e.g., organometallic reactions.[3,7] Glass samples provide rigidity and environmental stability; however, they have a broad NC size distribution (typically greater than 20%) and a large number of surface defects. A much higher level of synthetic flexibility and control is provided by colloidal NCs which can be chemically manipulated in a variety of ways including size-selective techniques[7] (resulting in less than 5% size variations), surface modification by exchanging the passivation layer,[8,9] formation of layered NC heterostructures,[10,11] immobilization in sol−gel[12] and polymer[13] matrices, and self-assembly into 3D superlattices.[14,15]

The focus of this review is studies of ultrafast carrier dynamics and band-edge optical nonlinearities in colloidal NCs. Because of a large energy level spacing and an enhanced surface-to-volume ratio, carrier dynamics in NCs are significantly different from those in bulk materials. The large energy level separation has been predicted to significantly inhibit intraband energy relaxation due to a "phonon bottleneck"[16] which, however, has been argued against by recent experiments.[17,18] After initial fast energy redistribution, carrier relaxation in bulk II−VI semiconductors proceeds primarily by radiative decay. In NCs, carrier dynamics in this stage of relaxation can be much faster than for radiative decay due to enhancement of nonradiative processes associated, e.g., with surface trapping[18,19] and/or multiparticle Auger recombination.[20,21]

In NCs, band-edge optical nonlinearities arise primarily from state-filling leading to bleaching of optical transitions and Coulomb multiparticle interactions resulting in transition shifts and modifications in transition oscillator strengths.[22] Because thermal depopulation of the lowest quantized states is inhibited by a large separation between energy levels, the role of state filling in NCs is enhanced in comparison with that in bulk materials. Coulomb effects are also enhanced in small-size NCs, due to a $1/R$ scaling (R is the NC radius) of the Coulomb potential. Further enhancement in nonlinearties caused by Coulomb electron−hole (e−h) interactions can occur as a result of surface trapping of one type of carriers (electrons or holes) leading to generation of strong local fields.[23]

The article begins with analysis of linear and nonlinear (transient) absorption spectra of CdSe NCs (sections 2 and 3) which allows us to quantify the size dependence of NC linear and nonlinear absorption cross sections and to evaluate the role of different mechanisms for optical nonlinearities. This analysis is followed by an overview of studies of intraband energy relaxation with a special emphasis on the role of nonphonon mechanisms for energy losses (section 4). Finally, we review studies of electron and hole dynamics in the stage following initial energy relaxation for both single and multiple e−h pair regimes (section 5).

† E-mail: klimov@lanl.gov.

10.1021/jp9944132 CCC: $19.00
Published on Web 06/06/2000

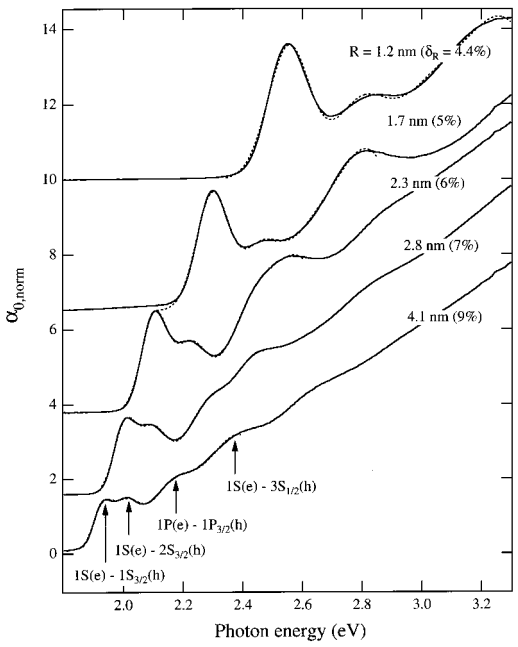

Figure 1. Linear absorption spectra of TOPO/TOPSe-passivated CdSe NCs with radii from 1.2 to 4.1 nm (solid lines) fit to a sum of four Gaussian bands (dotted lines). NC size dispersions derived from the fits are indicated in parentheses. Arrows mark the positions of the four well-resolved transitions involving 1S and 1P electron states in the 4.1 nm sample.

2. Linear Absorption Spectra and Absorption Cross Sections of CdSe Nanocrystals

This review concentrates on CdSe colloidal NCs fabricated by organometallic synthesis.[7] As prepared, these NCs are passivated with organic molecules of trioctylphosphine oxide (TOPO) and trioctylphosphine selenide (TOPSe).[9] The capping layer prevents nanoparticles from aggregating and renders them soluble. It also provides a varying degree of "electronic" passivation of surface traps as discussed in section 5.1. The original passivation can be modified via surface exchange reactions,[7,9] which has been used in studies of the influence of surface treatment on the electronic and optical properties of NCs.[9,24,25] In addition to passivation with organic molecules, CdSe NCs can be overcoated with a layer of a wide-gap inorganic semiconductor such as ZnS.[11] This allows one to greatly improve "electronic" passivation of NC surfaces, resulting, in particular, in a significant increase in the photoluminescence (PL) quantum yield.

We will review room temperature results for CdSe NCs with mean radii from 1 to 4 nm and a size dispersion from 4% to 9%. Since the exciton Bohr radius in CdSe is ~5 nm, this size range corresponds to the regime of extremely strong confinement for which the spacing between the two lowest electron states (>200 meV) is much greater than both the exciton binding energy (16 meV) and the energy of the longitudinal optical (LO) phonon (26 meV).

In Figure 1, we show linear absorption spectra (α_0) of five colloidal samples with NC radii 1.2, 1.7, 2.3, 2.8, and 4.1 nm. Because of a narrow NC size distribution, these spectra show well-resolved features corresponding to interband optical transitions coupling different electron and hole quantized states. The detailed PL-excitation studies of ref 26 demonstrate that these features can be explained by the effective-mass model, taking into account confinement-induced mixing of three valence subbands.[27] In this model, electron states are labeled using a letter (l) to denote the angular momentum of the envelop wave function (S for $l = 0$, P for $l = 1$, D for $l = 2$, etc.) and the digit to denote a number of the state of a given symmetry. The electron states are $2(2l + 1)$-fold degenerate with respect to the spin projection and the projection of the angular momentum of the envelop wave function. The three lowest electron states in the order of increasing energy are 1S, 1P, and 1D. The notation for hole states is similar to that used for electron states, with the addition of a subscript which denotes the total hole angular momentum (F), which is the sum of the valence-band Bloch-function momentum and the momentum of the hole envelope wave function.[27,28] The hole states are $(2F + 1)$-fold degenerate. This degeneracy is lifted if the effects of the crystal field in a hexagonal lattice,[29] NC nonspherical shape,[30] and exchange interactions[31,32] are taken into account, leading to a fine structure of the lowest exciton state.[32] In CdSe NCs with $R > 2$ nm, the first three hole states in the order of increasing energy are $1S_{3/2}$, $1P_{3/2}$, $2S_{3/2}$.[27]

The two lowest bands in the linear absorption spectra in Figure 1 can be assigned to transitions involving the lowest electron state (1S) and two different hole states ($1S_{3/2}$ and $2S_{3/2}$). In the following, we will refer to these transitions as 1S [1S(e)−$1S_{3/2}$(h)] and 2S [1S(e)−$2S_{3/2}$(h)]. The linear absorption spectra of NCs with $R > 2.5$ nm also exhibit a well-resolved band associated with the transition coupling the 1P electron state to the $1P_{3/2}$ hole state (1P transition) and a higher-lying band associated with the transition involving the 1S electron state and a hole state originating from the spin−orbit split-off band ($3S_{1/2}$ for NC with $R = 4.1$ nm). In 4.1 nm NCs, the latter band is also contributed by the transition involving the 1D electron state (see section 3.3).

The broadening of optical transitions observed in the absorption spectra of colloidal NCs is primarily due to inhomogeneity arising from size dispersion. In the strong-confinement regime, the size dependence of energy transitions in NCs is dominated by a term proportional to $1/R^2$. In this case, the inhomogeneous broadening (Γ_i) of the transition with energy $\hbar\omega_i$ is proportional to the shift of this transition with respect to the bulk material energy gap (E_g). For a Gaussian size distribution with a standard deviation Δ_R

$$\Gamma_i = \frac{2\Delta_R}{R}(\hbar\omega_i - E_g) = 2\delta_R\Delta_i \qquad (1)$$

where $\Delta_i = \hbar\omega_i - E_g$ and $\delta_R = \Delta_R/R$. For NCs with $R = 1.7$ nm ($\Delta_{1S} = 550$ meV) and $\delta_R = 5\%$, we calculate $\Gamma_{1S} = 55$ meV, which corresponds to about 130 meV width of the 1S absorption peak measured at the half-amplitude. This is consistent with the width of the lowest transition (140 meV) derived from the linear absorption spectrum of the 1.7 nm sample (see Figure 1).

In Figure 2a, we show a semilogarithmic plot of linear absorption spectra recorded over the range ~1.8−4.8 eV for the same set of samples as in Figure 1. The spectra are normalized to match absorption coefficients at high spectral energies. In all samples, distinct optical transitions are well resolved within about 1 eV on the high-energy side of the 1S resonance. At higher spectral energies, due to the increasing spectral density of electron and hole quantized states, the optical transitions merge into a structureless profile which has essentially the same spectral shape for all samples independent of their sizes. Interestingly, at $\hbar\omega \geq 3.5$ eV, the absorption spectra of NCs closely match the bulk CdSe absorption spectrum[33] corrected for local fields effects.[34] The spectrum of the correction factor $|\eta|^2$ (inset to Figure 2a) was calculated using the bulk CdSe spectral data (ref 33) and therefore does

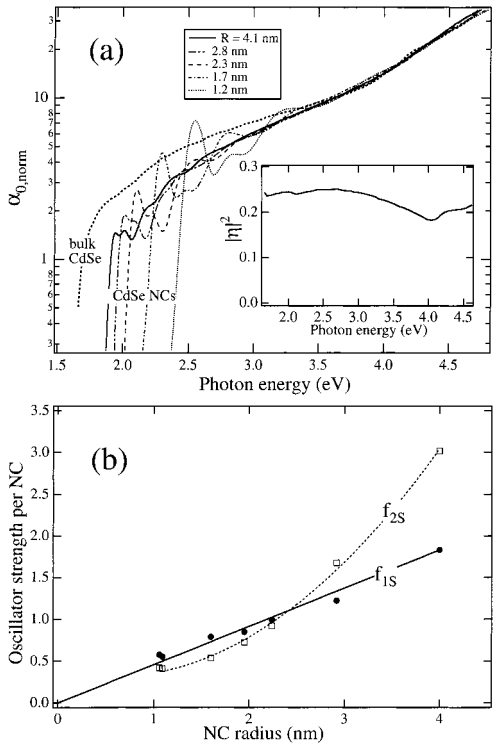

Figure 2. (a) Normalized linear absorption spectra of CdSe NCs with radii from 1.2 to 4.1 nm in comparison to the absorption spectrum of bulk CdSe corrected for local field effects. The spectrum of the correction factor $|\eta|^2$ is shown in the inset. (b) NC size dependence of oscillator strengths of the 1S and 2S transitions derived from normalized spectra in the upper panel.

not account for a discreteness of NC optical transitions. Thus, it provides an accurate description of local field effects only at high spectral energies for which the NC transitions merge into a bulklike structureless absorption.

The fact that absorption spectra of NCs of different sizes converge at large $\hbar\omega$ into the bulk-semiconductor spectrum indicates that at high spectral energies the optical absorption of NC samples is NC size independent and is only determined by the amount (volume fraction ξ) of the semiconductor material, which is consistent with predictions of a simple effective-mass theory.[1] This result can be expressed by the following formula:

$$\alpha_0(\hbar\omega \geq 3.5\ \text{eV}) = \xi|\eta(\hbar\omega)|^2\alpha_b(\hbar\omega) = n_0V_0|\eta(\hbar\omega)|^2\alpha_b(\hbar\omega) \quad (2)$$

where $\alpha_b(\hbar\omega)$ is the bulk material absorption, V_0 is the volume of a single NC, and n_0 is the NC concentration in the sample. Equation 2 results in the following expression for the NC absorption cross section $\sigma_0 = \alpha_0/n_0$:

$$\sigma_0(\hbar\omega \geq 3.5\ \text{eV}) = V_0|\eta(\hbar\omega)|^2\alpha_b(\hbar\omega) = \frac{4\pi}{3}R^3|\eta(\hbar\omega)|^2\alpha_b(\hbar\omega) \quad (3)$$

which indicates a strong NC size dependence of σ_0 ($\sigma_0 \propto R^3$). Scaling eq 3 according to the experimentally measured absorption spectra of NC samples, one can calculate absorption cross sections at low spectral energies, i.e., in the range where eq 3 is invalid. For example, at 3.1 eV (this corresponds to the pump photon energy in all femtosecond (fs) experiments described below), this procedure gives the following numerical expression: $\sigma_0\ (\text{cm}^2) = 1.6 \times 10^{-16}[R\ (\text{nm})]^3$.

The normalized spectra in Figure 2a can be used to derive the size dependence of absorption cross sections (oscillator strengths) of the low-energy 1S and 2S transitions which are observed as distinct "quantized" bands for all NC sizes from 1 to 4 nm. The scaling procedure to match absorption of NCs of different sizes at high-spectral energies, applied to the spectra in Figure 2a, is equivalent to adjusting the volume fraction of semiconductor to be the same for all samples: $\xi = V_0n_0 = \text{const}$. Thus, the normalized spectra in Figure 2a can be considered as taken for a set of samples for which the NC concentration varies proportional to R^{-3}. Therefore, the transition areas derived from these spectra and scaled by R^3 provide a measure of the size-dependent oscillator strength per single NC.

In order to accurately find the areas of the 1S and 2S transitions, we performed a deconvolution of the low-energy portion of the spectra using a sum of four Gaussian bands (dotted lines in Figure 1):

$$\alpha_0(\hbar\omega) = \sum_{i=1}^{4}\frac{a_i}{\sqrt{2\pi}\Gamma_i}\exp\left[-\frac{(\hbar\omega - \Delta_i)^2}{2\Gamma_i^2}\right] \quad (4)$$

where a_i is the area of the $\hbar\omega_i$ transition, and Γ_i is the transition broadening which is assumed to scale with the transition energy according to eq 1. The size-dependent oscillator strengths ($f_i \propto a_iR^3$) derived using this procedure are displayed in Figure 2b. For both the 1S and 2S transitions, the oscillator strength shows a strong size dependence. In the size range studied (1−4 nm), this dependence is linear for the 1S transition ($f_{1S} \propto R$) and quadratic for the 2S transition.

Equation 4 indicates that the amplitude of the 1S absorption cross section [$\sigma_0(1S)$] can be expressed as proportional to f_{1S}/Γ_{1S}. Taking into account the linear size dependence of f_{1S} found experimentally (Figure 2b), we can derive the following expression for $\sigma_0(1S)$: $\sigma_0(1S) \approx \beta R/\Gamma_{1S}$, where $\beta = 1.5 \times 10^{-14}$ cm^2 meV nm^{-1}, as found by scaling eq 3 by the factor of $\alpha_0(1S)/\alpha_0(3.5\ \text{eV})$ which was calculated using experimental data. Thus, the 1S absorption cross section exhibits a much weaker size dependence ($\propto R$) than the absorption cross sections at high spectral energies ($\propto R^3$). This difference arises from an increased overlap of optical transitions with increasing transition energy which occurs due to an increased spectral density of quantized states. As a result, the size dependence of high-spectral-energy absorption cross sections is significantly affected by size-dependent changes in both the oscillator strength of an individual transition and the spectral density of optical transitions.

3. Resonant Optical Nonlinearities in Semiconductor Nanocrystals

3.1. Mechanisms for Ultrafast Optical Nonlinearities. Time-resolved nonlinear optical spectroscopy is a powerful tool for studies of energy structures and carrier dynamics in different classes of bulk and low-dimensional materials.[22,35] In this article we will concentrate on optical nonlinearities resulting from photoexcitation of "real" carrier populations, which are often referred to as resonant nonlinearities. In NCs, resonant optical nonlinearites are primarily due to state filling and Coulomb multiparticle interactions (the carrier-induced Stark effect).[22]

In NCs, state filling leads to bleaching of the interband optical transitions involving populated quantized states. The absorption changes resulting from this effect are proportional to the sum of the electron and hole occupation numbers. If we present the linear absorption spectrum of NCs as a sum of separate absorption bands corresponding to different "quantized" optical

transitions, the state-filling induced absorption changes ($\Delta\alpha$) can be calculated using the expression:

$$\Delta\alpha(\hbar\omega) = -\sum_i a_i G_i(\hbar\omega - \hbar\omega_i)(n_i^e + n_i^h) \qquad (5)$$

where $G_i(\hbar\omega - \hbar\omega_i)$ is the unit-area absorption profile of the $\hbar\omega_i$ transition, a_i is the transition area (proportional to its oscillator strength), and n_i^e and n_i^h are occupation numbers of electron and hole states involved in the transition. Under thermal quasi-equilibrium (after the intraband relaxation is finished), the occupation numbers can be found using the Fermi distribution function.

Because of degeneracy of the valence band and the large difference between electron and hole masses (in CdSe, $m_h/m_e \approx 6$), the room-temperature occupation probabilities of electron states are much greater than those of the coupled hole states (the hole populations are spread over many adjacent levels by the thermal distribution). As a result, the state-filling-induced absorption changes are dominated by electrons.[36] The role of holes in transitions' bleaching is further reduced because of the extremely fast depopulation of the initially excited valence-band states (subpicosecond (sub-ps) to picosecond (ps) time scales), typical for all II−VI NC samples.[37,38] The role of holes in state-filling-induced signals is discussed in more detail in section 3.3 in the context of studies of the pump dependence of absorption bleaching.

In addition to state filling, photoexcitation of carrier populations leads to generation of local fields, which modify the optical spectra of NCs due to the Stark effect. The Stark effect leads to a shift of optical transitions and changes in transitions oscillator strengths due to modifications in selection rules. In terms of traditional pump−probe spectroscopy (see section 3.2), the carrier-induced Stark effect can be interpreted as arising from Coulomb interactions between one or several e−h pairs excited by the pump pulse and the e−h pair generated by the probe pulse. In contrast to state filling which *selectively* affects only transitions involving populated states, the carrier-induced Stark effect does not have this selectivity and modifies all NC transitions.[39] The Stark effect is particularly important in the case of charge separated e−h pairs which can be formed, for example, as a result of surface trapping of one type of carriers (the trapped-carrier induced Stark effect).[23] In the case of two interacting e−h pairs, it can be considered as arising from biexciton Coulomb interactions,[39−41] and the transition Stark shift can be used as a measure of the binding energy of the 3D-confined biexciton. Spatial confinement leads to an enhancement in the biexciton binding energy in comparison with that in bulk materials.[40] In bulk CdSe, the biexciton binding energy is only about 4 meV,[42] whereas in small size CdSe NCs it is in the tens of millielectronvolts range.[39,41]

In the case of an isolated optical transition, and in the limit of small fields (the Stark shift Δ_S is small in comparison with the transition broadening Γ), absorption changes due to the Stark effect can be calculated as proportional to the first derivative of the linear absorption spectrum: $\Delta\alpha(\hbar\omega) \approx \Delta_S\alpha'_0(\hbar\omega)$. In the presence of two closely spaced broad transitions (energy spacing $\Delta_{12} < \Delta_S$, and $\Delta_{12} < \Gamma$), the Stark effect leads to a repulsion between the transitions, with an associated absorption change which can be approximated by a second derivative of the absorption profile: $\Delta\alpha(\hbar\omega) \approx \Delta_S\Delta_{12}\alpha''_0(\hbar\omega)$. This second limit is likely apply to NCs, because large carrier-induced Stark shifts should lead to strong interactions between closely-spaced NC valence band states.[23]

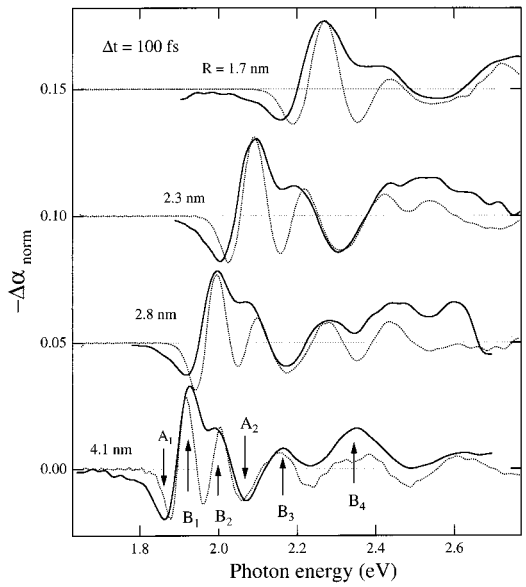

Figure 3. Early-time TA spectra ($\Delta t = 100$ fs) of CdSe NCs with radii from 1.7 to 4.1 nm (solid lines) in comparison to the second derivative of the absorption spectra (dotted lines).

3.2. Femtosecond Dynamics of Transient Absorption Spectra. To study carrier-induced absorption changes, we used a high-sensitivity femtosecond transient absorption (TA) pump−probe experiment.[43] The samples were pumped at 3.1 eV by frequency-doubled 100 fs pulses from an amplified Ti−sapphire laser. The pump-induced absorption changes were probed over the range from 1.3 to 3 eV with a femtosecond white-light continuum generated in a sapphire plate. In the case of time-resolved sub-ps measurements, it is important to account for temporal dispersion of the frequency (chirp) of the probe pulse.[44] To perform chirp-free TA measurements, we used single-wavelength phase-sensitive detection and spectral scanning, with simultaneous adjustment of the time delay between pump and probe pulses. This technique allows chirp-free, high-sensitivity detection of TA signals with an accuracy up to 10^{-5} in differential transmission.[43]

In Figure 3, we show the chirp-free TA spectra of a series of CdSe nanocrystals with radii from 1.7 to 4.1 nm detected at the pump−probe delay $\Delta t = 100$ fs. These spectra were taken at low pump intensities corresponding to initial NC populations $\langle N_0\rangle$ less than one e−h pair per NC on average. $\langle N_0\rangle$ can be calculated as $\langle N_0\rangle = \Phi_p\sigma_0$, where Φ_p is the pump fluence (presented in photons/cm^2) and σ_0 is the NC absorption cross section at the pump wavelength (see section 2). The shape of the early-time TA spectra (solid lines in Figure 3) is similar to that of the second derivative of the absorption spectra (dotted lines in Figure 3), which is consistent with the Stark effect in the system of closely spaced broad transitions.[23] At pump densities such that $\langle N_0\rangle < 1$, this effect can be described in terms of the two-pair (biexciton) interactions.[39−41]

The carrier-induced Stark effect is manifested in TA spectra as bleaching features ($\Delta\alpha < 0$) at the positions of the "original" transitions (i.e., transitions seen in linear absorption) and photoinduced absorption (PA) features ($\Delta\alpha > 0$) at the positions of the "new" (shifted) transitions. For NCs with $R = 4.1$ nm, the bleaching bands B_1, B_2, B_3, and B_4 (Figure 3) can be assigned to the 1S, 2S, 1P, and 1S(e)−3S$_{1/2}$(h) transitions, respectively (compare spectra in Figures 1 and 3). The band B_4 is also contributed by the transition involving the 1D electron state (see discussion of pump-dependent TA spectra in section 3.3). In Figure 3, one can also resolve PA features A_1 (a low-

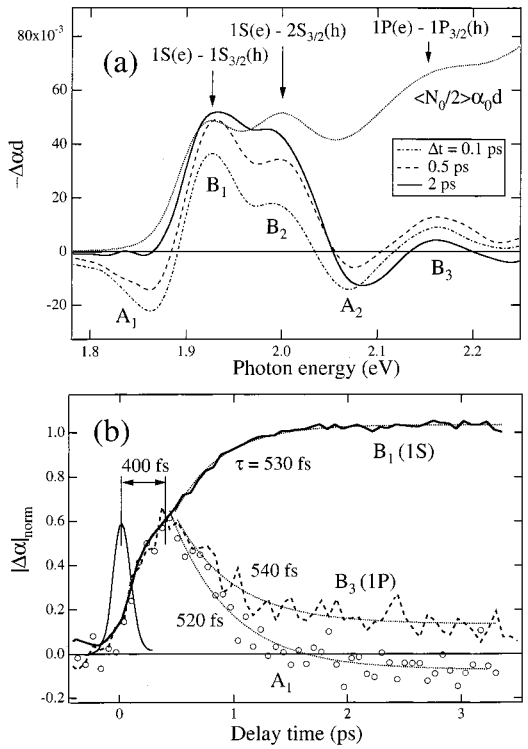

Figure 4. (a) TA spectra of CdSe NCs (R = 4.1 nm) recorded at 0.1, 0.5, and 2 ps after excitation in comparison to the linear absorption spectrum scaled by the NC population factor $\langle N_0/2 \rangle$. (b) TA dynamics at the positions of the B_1 (thick solid line), B_3 (thick dashed line), and A_1 (circles) features, fit to a single-exponential growth/decay (thin dotted lines). Thin solid line is the pump−probe cross-correlation.

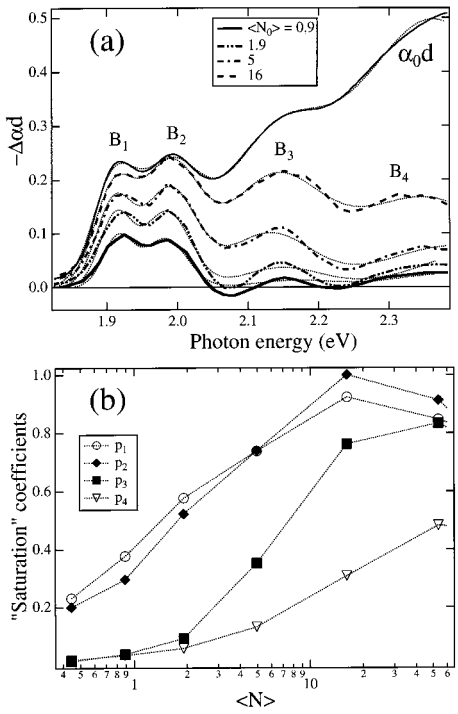

Figure 5. (a) Pump-dependent TA spectra (thick lines) of CdSe NCs with R = 4.1 nm taken at Δt = 2 ps in comparison to the linear absorption spectrum (thin solid line). Thin dotted lines are fits to a sum of four Gaussian bands (see text for details). (b) Pump dependence of the p_1−p_4 "saturation" coefficients (normalized B_1−B_4 bleaching areas) derived from fits to the spectra in the upper panel.

energy shift of the 1S transition) and A_2 (a low-energy shift of the 1P transition and/or a high-energy shift of the 2S transition).

The contribution of state filling to band-edge signals at $\Delta t \leq 100$ fs is not significant, because low-energy states remain unpopulated until 150−600 fs after excitation (see section 4.1). With increasing the time Δt, carriers relax into low-energy quantized states, leading to increasing contribution from state filling to the band-edge absorption changes. This effect is illustrated in Figure 4 by time-resolved spectra (a) and dynamics (b) of $\Delta\alpha d$ (d is the sample thickness) recorded for the 4.1 nm sample. The 0.1 ps TA spectrum is entirely due to the carrier-induced Stark effect (compare the TA spectrum and the second derivative of the absorption spectrum of the 4.1 nm sample in Figure 3). At 0.5 ps, we observe the growth of B_1, B_2, and B_3 features due increasing population of the 1S and 1P electron states, resulting in an increased state-filling effect. In the 2 ps spectrum, the B_1 feature is further increased, whereas the amplitude of the B_3 feature decreases, which is due to relaxation of the 1P electrons into the lower 1S state. This interpretation is consistent with TA dynamics in Figure 4b.

The B_3 feature (thick dashed line in Figure 4b) is delayed by about 400 fs with respect to the pump pulse which is roughly the time of the electron relaxation into the 1P state. The decay of this feature is very fast and occurs with a 540 fs time constant, which corresponds to the time of the 1P-to-1S electron relaxation[18] (see discussion of energy relaxation in section 4.1). The dynamics of B_1 show a fast initial rise due to the biexciton effect, followed by a slower signal increase with a 530 fs time constant (thick solid line in Figure 4b). The secondary B_1 growth is complementary to the B_3 decay and is associated with increasing 1S population, due to relaxation of electrons from the 1P state. Interestingly, the buildup of the B_1 band is accompanied by the decay of the A_1 feature (circles in Figure 4b), associated with the transition Stark shift. This indicates that the dynamics of A_1 are also related to carrier intraband relaxation, and can be understood as occurring due to the large bandwidth of optical transitions leading to a significant contribution of the 1S bleaching even at large detunings from the center of the B_1 band. Therefore, the increasing bleaching of the 1S transition accompanying carrier energy relaxation overwhelms the A_1 PA feature as the 1S state becomes occupied (see ref 39 for a numerical analysis of a competition between state filling and the Coulomb-interaction-induced transition shifts).

3.3. Pump Dependence of Band-Edge Bleaching Signals. After the energy relaxation is finished and the 1S electron state is populated, the 1S bleaching is due to both the Stark effect and state filling. If the 1S state is only filled with one electron (this corresponds to the pump regime $\langle N_0 \rangle < 1$), state filling completely saturates one of the two spin-degenerate 1S transitions, whereas the absorption changes for the unpopulated transition are due to the Stark effect. State-filling-induced signal within the 1S and 2S transitions can be estimated from the product of the population factor $n_{1S}^{e} = \langle N_0 \rangle/2$ and α_0. Comparison of this product (dotted line in Figure 4a) with the 2 ps TA spectrum indicates that state filling provides a dominant contribution to $\Delta\alpha$ within the B_1 and B_2 bands.

The relative contribution of state filling to transitions bleaching increases with increasing the average NC populations which is obvious from pump-dependent TA spectra in Figure 5a (Δt = 2 ps). In the spectrum taken at $\langle N_0 \rangle = 0.9$ one can still discern weak PA features due to the Stark effect. However, at pump levels above $\langle N_0 \rangle \approx 2$, we observe bleaching over the entire spectral range from B_1 to B_4. To analyze pump-dependent $\Delta\alpha d$ spectra, we fit them to a sum of four Gaussian bands (see eq 4) which account for the B_1−B_4 bleaching features. The positions and the widths of the bands were derived by fitting the linear

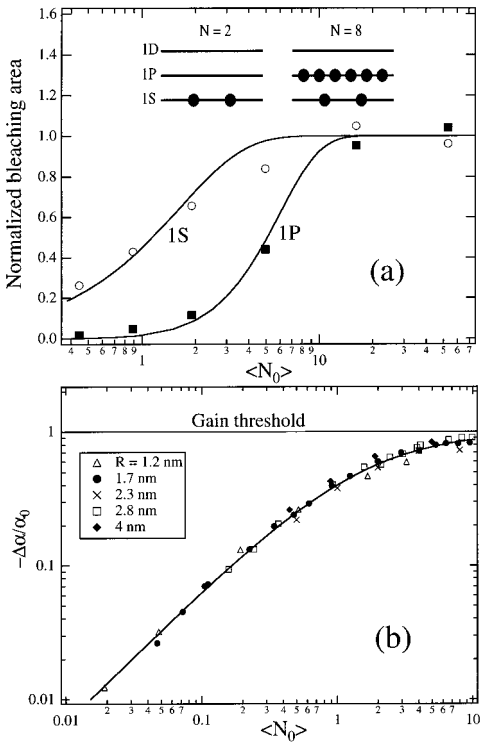

Figure 6. (a) Pump dependence of the normalized 1S and 1P bleaching areas (symbols) in comparison to the pump-dependent average occupation numbers of the 2-fold-degenerate 1S and the 6-fold-degenerate 1P electron states calculated assuming a "Poisson" type population growth (lines). (b) Pump dependence of normalized 1S absorption changes for NCs of different sizes (symbols) fit to the "universal" pump dependence $-\Delta\alpha/\alpha_0 = k_1\langle N_0\rangle/(k_2 + \langle N_0\rangle)$, with $k_1 = 1.05$ and $k_2 = 1.6$ (line).

absorption spectrum and were kept fixed during the fit of the bleaching data. The transitions areas were presented as $a_i = p_i a_{0i}$, where a_{0i} are the areas of transitions in the linear absorption spectrum and $p_i(\langle N\rangle)$ are "saturation" coefficients describing the pump-dependent transition bleaching. In terms of the state filling model, these coefficients account for the population factors in eq 5: $p_i = n_i^e + n_i^h \approx n_i^e$.

The pump-density dependence of p_i is shown in Figure 5b. This dependence is almost identical for p_1 and p_2, as expected for the 1S and 2S transitions which are bleached due to a population increase of the same 1S electron state. The p_3 shows a delayed growth with the onset at $\langle N_0\rangle \approx 2$, which is consistent with the threshold expected for the filling of the 1P electron level. The growth of p_4 is further delayed (the onset ~5), indicating the beginning of the filling of the next (1D) electron level.

In Figure 6a, we compare the pump dependence of the normalized "saturation" coefficients p_1 (circles) and p_2 (squares) with pump-dependent occupation numbers of the 1S and 1P electron states calculated within the state-filling model (lines). In the case where the pump photon energy is much greater than the NC energy gap (this corresponds to our experimental situation), carrier-induced absorption saturation at the pump wavelength is insignificant, and the probability of generation of the e−h in a NC is independent of the number of pairs already existing in it. This assumption results in the Poisson distribution of NC populations: $P(N) = \langle N\rangle^N e^{-\langle N\rangle}/N!$, where $P(N)$ is the probability of having N e−h pairs in a selected NC when the average population of NCs is $\langle N\rangle$. The occupation numbers of the 1S and 1P states in this model can be calculated as follows: $n_{1S}^e = 0.5P(1) + \sum_{i=2}^{\infty} P(i)$, $n_{1P}^e = \sum_{i=3}^{7} P(i)(i-2)/6 + \sum_{i=8}^{\infty} P(i)$. The pump dependence of the calculated occupation numbers (lines in Figure 6a) matches closely the dependence measured for "saturation" coefficients (symbols in Figure 6a). This is strong evidence that bleaching of NC transitions involving occupied states is primarily due to state filling, and that this effect is dominated by populations of electron quantized states. The data in Figure 6a is also an illustrative demonstration of a sequential filling of electron shells in QD "artificial" atoms, which is analogous to filling of electron orbitals in atoms of "natural" elements.

In order to establish an accurate relationship between the magnitude of TA signals and NC average populations, we analyzed the pump dependence of the 1S bleaching measured immediately after the intraband relaxation is finished (Δt from 1 to 2 ps) for NCs of different sizes. Interestingly, if we normalize the magnitude of the 1S bleaching by the 1S linear absorption, in the plot $-\Delta\alpha/\alpha_0$ vs $\langle N_0\rangle$, the data points for all samples fall along one "universal" curve, independent of NC sizes (see Figure 6b, symbols). This curve shows a linear growth at low pump intensities ($\langle N_0\rangle < 0.5$) and saturates as $-\Delta\alpha/\alpha_0$ approaches unity at high pump densities. This "universal" behavior can be described by the dependence

$$-\Delta\alpha/\alpha_0 = k_1\langle N_0\rangle/(k_2 + \langle N_0\rangle) \quad (6)$$

with $k_1 = 1.05 \pm 0.15$ and $k_2 = 1.6 \pm 0.3$ (line in Figure 6 b). This dependence allows one to accurately determine instant NC populations from the measured $\Delta\alpha$ dynamics which is used, for example, in section 5.2 in the analysis of the Auger effects.

Simple two-level-system arguments predict the 1S optical gain at $\langle N_0\rangle > 1$ in the case of both electrons and hole contributing to the 1S bleaching.[38] However, none of the samples in Figure 6b shows a crossover from absorption to gain at the position of the 1S transition. The maximum $\Delta\alpha$ measured experimentally corresponds to the complete bleaching of the 1S tranistion ($\Delta\alpha \approx \alpha_0$), which has been predicted for the case of only electrons contributing to the state-filling-induced signals.[38] This provides an additional piece of evidence that in NCs, the state-filling-induced bleaching at room temperature is primarily due to electron populations.

4. Intraband Energy Relaxation in Semiconductor Nanocrystals

4.1. NC Size Dependence of Intraband Relaxation Rates. In bulk II−VI semiconductors, carrier energy relaxation is dominated by the Fröhlich interactions with longitudinal optical (LO) phonons, leading to fast (typically sub-ps) carrier cooling dynamics.[45−47] In NCs, even in the regime of weak confinement when the level spacing is only a few millielectronvolts, the carrier relaxation mediated by interactions with phonons is hindered dramatically because of restrictions imposed by energy and momentum conservation leading to a phenomenon called a "phonon bottleneck".[16,48] Further reduction in the energy loss rate is expected in the regime of strong confinement, for which the level spacing can be much greater than LO phonon energies, and hence carrier-phonon scattering can only occur via weak multiphonon processes.

Despite these theoretical predictions, a number of recent experimental results indicate that carrier relaxation in II−VI NCs is not significantly slower than in bulk materials.[17,37,39,49] Strong evidence against the existence of the phonon bottleneck in 3D confined systems has been obtained in recent studies of intraband relaxation in CdSe NCs[18,50] which indicate sub-ps 1P-to-1S electron relaxation even in NCs for which the 1S−1P

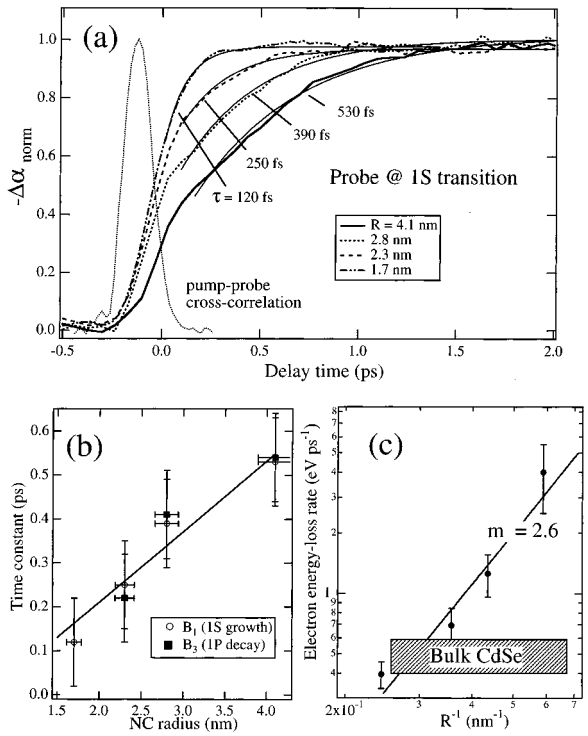

Figure 7. (a) The 1S-bleaching build-up dynamics in CdSe NCs with radii 1.7, 2.3, 2.8, and 4.1 nm (thick lines), fit to a single-exponential growth (thin solid lines). The thin dotted line is the pump−probe cross-correlation. (b) The NC-size dependence of time constants of the 1P decay (squares) and the 1S growth (circles) in comparison to a linear fit (line). (c) Size dependence of the electron energy-loss rate in CdSe NCs (symbols) in comparison to the $R^{-2.6}$ fit (line). The shaded region shows the range of energy-loss rates characteristic of the electron−LO−phonon scattering in bulk CdSe.

energy separation is greater than 10 LO phonon energies. The results of these studies are reviewed below.

As pointed out in the discussion of femtosecond TA signals in section 3.2, the decay of the 1P bleaching (B_3 in Figure 4a) and the complementary growth of the 1S bleaching (B_1 in Figure 4a) provide a measure of the rate of the 1P-to-1S energy relaxation. For 4.1 nm NCs, this relaxation is extremely fast and occurs with a 540 fs time constant (Figure 4b). This fast relaxation occurs despite the fact that the 1S−1P energy separation is about eight LO phonon energies, which makes the probability of the direct multiphonon emission negligibly small. Interestingly, intraband relaxation becomes faster with decreasing NC size. This is obvious from Figure 7a in which we compare the 1S state population dynamics in NCs of different radii. These data indicate a decrease in the 1S buildup time with decreasing NC radius. This time shortens from 530 fs for R = 4.1 nm to 120 fs for R = 1.7 nm, roughly following a linear dependence (Figure 7b).

In Figure 7c, we compare size-dependent rates of energy relaxation (dE_e/dt) observed in NCs with the energy-relaxation rate characteristic of the electron−LO−phonon scattering in bulk CdSe (shaded region in Figure 7c).[50] In 4.1 nm NCs, the energy-loss rate is ~0.44 eV ps^{-1}, which is essentially the same as in the bulk material, but many orders of magnitude greater than the rate expected for a multiphonon emission.[51] The energy-loss rate rapidly increases (roughly as $R^{-2.6}$) with decreasing NC size (Figure 7c). For NCs with R = 1.7 nm, it is ~4 eV ps^{-1}, which is almost an order of magnitude greater than for LO phonon emission in bulk materials.

Extremely fast electron relaxation, as well as a confinement-induced enhancement in the relaxation process, clearly indicates that energy relaxation in NCs is dominated by *nonphonon* energy-loss mechanisms. Recent works have suggested that coupling to defects,[52] Auger interactions with carriers outside the NC,[53] or Auger-type e−h energy transfer[54] can lead to fast energy relaxation not limited by a phonon bottleneck. The first two of these mechanisms are not intrinsic to NCs and cannot explain relaxation data for colloidal samples.[50] These data indicate that in colloidal nanoparticles, energy relaxation does not show any significant dependence on NC surface properties (i.e., the number of surface defects) and remain almost identical for different liquid- and solid-state matrices, including transparent optically-passive glasses, polymers, and organic solvents, for which no carriers is generated outside the NC.

The energy-loss mechanism proposed in ref 54 involves transfer of the electron excess energy to a hole, with subsequent fast hole relaxation through its dense spectrum of states. This mechanism is based on the intrinsic Auger-type e−h interactions and leads to significantly faster relaxation times than those for the multiphonon emission. To evaluate the role of e−h interactions in intraband energy relaxation, we studied electron intraband dynamics as a function of the e−h spatial separation.[55]

4.2. Electron−Hole Interactions and Intraband Energy Relaxation. Due to a large surface-to-volume ratio, electron and hole wave functions in NCs are strongly affected by NC surface properties, which can be used, for example, to spatially separate electrons and holes by passivating NCs with electron-accepting[56] or hole-accepting[25,55] molecules. We studied the 1P-to-1S relaxation in ZnS- and pyridine-passivated CdSe NCs. A ZnS surface layer creates a confining potential for both electrons and holes. Therefore, in ZnS-capped NCs, the e−h coupling should not significantly change during electron/hole relaxation. The pyridine acts as an efficient hole acceptor. As a result, in pyridine-passivated NCs, the e−h coupling is strong immediately after photoexcitation and is reduced dramatically after the hole is transferred to a capping group. This should have a strong effect on electron intraband relaxation, if it is indeed due to the e−h interactions.

In order to monitor electron intraband dynamics at different stages of hole relaxation/transfer, we used a three-pulse femtosecond TA experiment (Figure 8a), in which the sample was excited by a sequence of two ultrashort pulses (one in the visible and another in the infrared (IR) spectral ranges) and was probed by broad-band pulses of a femtosecond white-light continuum. The visible interband pump (3.1 eV photon energy; 100 fs pulse duration) was used to create an e−h pair in the NC, whereas a time-delayed intraband IR pump (tunable within 0.49−1.1 eV; 250 fs pulse duration) was used to re-excite an electron within the conduction band. Pump-induced absorption changes were detected over the range 1.2−3 eV using a chirp-free phase-sensitive technique[43] with a lock-in amplifier synchronized to either chopped visible or chopped IR pump beams. Signals obtained by modulation of the visible pump provide information on absorption changes induced by either interband excitation alone (IR pump is "off"), or by combined inter- and intraband excitations (IR pump is "on"). Modulating the IR pump beam, one can directly detect changes in the *interband* TA due to the *intraband* re-excitation. A similar experiment but using a single IR wavelength for both the probe and the postpump was reported previously in ref 25.

In Figure 8b, we show 1S bleaching dynamics in ZnS-capped NCs (R = 1.15 nm) recorded with modulation of either the visible pump (dashed line (IR pump is off) and solid line (IR pump is on)) or the IR pump (circles). The delay between the visible and IR pump pulses (Δt_{IR}) was 0.6 ps. The IR pump

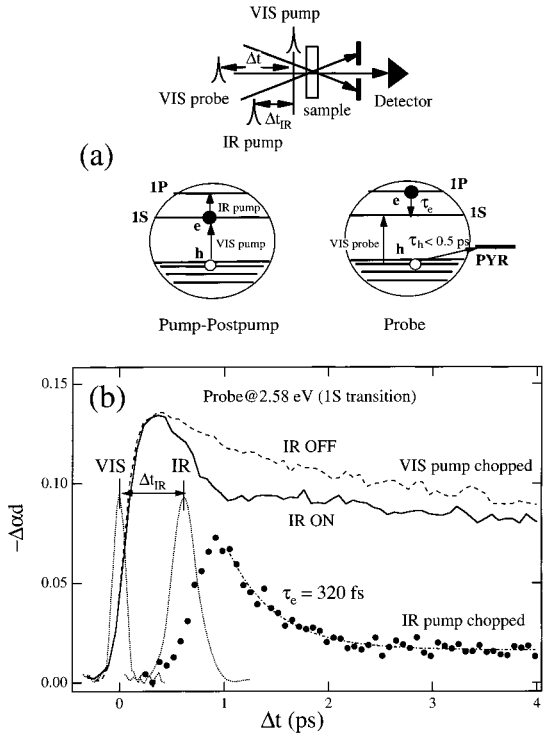

Figure 8. (a) Schematics of a three-pulse pump−probe experiment and the excitation/relaxation processes monitored in it. An e−h pair is created via an interband excitation with a pump pulse in the visible spectral range. The electron is re-excited within the conduction band by an IR postpump. The electron relaxation back to the ground state is monitored with a third pulse probing interband absorption changes. (b) The 1S bleaching dynamics recorded for ZnS-capped 1.15 nm CdSe NCs with (solid line) and without (dashed line) the IR postpump (modulation of the visible pump); dotted lines are cross correlations of the visible and IR pump pulses with a probe pulse. Circles are intraband electron dynamics recorded at the position of the 1S bleaching by modulating the IR postpump (the trace is scaled by a factor of −3); the dashed−dotted line is a single-exponential fit.

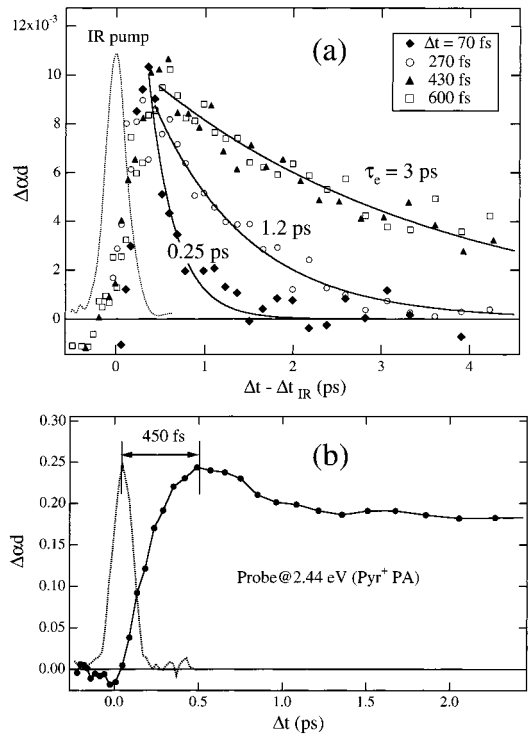

Figure 9. (a) Dynamics of the IR-postpump-induced 1S bleaching changes (electron intraband relaxation) in pyridine-capped 1.15 nm CdSe NCs detected at different delay times (Δt_{IR}) between the visible and IR pump which corresponds to different stages of hole transfer to a capping molecule (symbols are experimental data points, lines are single-exponential fits). (b) Dynamics of the pyridyne-cation-related PA (circles) detected in the traditional two-pulse pump−probe experiment. The dotted line is the pump−probe cross correlation.

was tuned to 0.55 eV which corresponded to the intra-conduction-band 1S−1P resonance. In the absence of the IR pump, the 1S bleaching shows a fast ∼150 fs growth followed by a monotonic nonexponential decay due to depopulation of the 1S electron state (dashed line). Application of the IR pulse leads to an abrupt decrease in the 1S bleaching due to re-excitation of the 1S electrons into the 1P state. A decay of perturbations associated with the IR pump provides a direct measure of the electron intraband relaxation back into the ground 1S state. To extract electron intraband dynamics one can either subtract time transients recorded with the IR pump "on" and "off", or to directly record them using a modulated IR beam (circles). Both approaches give the same result; however, the second method yields a better S/N ratio.

We monitored electron intraband dynamics for different delays between the visible and the IR pump pulses. For NCs with $R = 1.15$ nm studied in this work, the energy of the visible pump is almost resonant with the $1S(e)-2S_{3/2}(h)$ interband transition. Therefore, the electrons, which are generated directly in the lowest quantized 1S state, remain in this state until being re-excited by the IR pulse. On the other hand, holes, which initially populate the excited $2S_{3/2}$ state, can rapidly relax due to transitions into lower-energy quantized states inside the NC or the charge transfer to a capping group. Therefore, by varying the IR re-excitation time one can evaluate the effect of modification in the hole wave function (during hole relaxation/transfer) on electron intraband dynamics.

In ZnS-overcoated NCs (circles in Figure 8b), the 1P-to-1S relaxation is extremely fast (320 fs time constant) for all Δt_{IR} delays from 100 fs to 1 ps. In sharp contrast, in the pyridine-capped NCs (Figure 9a), electron dynamics show a strong dependence on the delay between visible and IR pulses. At $\Delta t_{IR} = 70$ fs (diamonds in Figure 9a), the relaxation constant is 250 fs, which is close to that in ZnS-capped NCs. With increasing the visible-IR pump delay, the electron relaxation time gradually increases up to 3 ps at $\Delta t_{IR} = 430$ fs (triangles in Figure 9a). A further increase in Δt_{IR} does not lead to significant changes in electron intraband dynamics (compare traces taken at $\Delta t_{IR} =$ 430 fs (triangles) and 600 fs (squares); Figure 9a).

Importantly, the threshold delay of roughly 400 fs found in three-pulse experiments is very close to the hole-transfer time to a capping molecule inferred from visible TA measurements of pyridine-capped NCs.[55] The pyridine cation (formed by hole transfer) is observed in TA spectra as a long-lived broad PA band below ∼2.5 eV which has a rise time of about 450 fs (Figure 9b). This strongly suggests that the dramatic changes in electron relaxation observed in pyridine-capped dots are due to changes in the e−h coupling, resulting from hole transfer to the capping group.

These data are consistent with the electron-relaxation mechanism involving Coulomb-interaction-mediated e−h energy transfer.[54] In the case of ZnS-capped samples, the holes are confined within the dot during the first 600 fs after excitation.[38] Therefore, the e−h coupling does change significantly on this time scale, consistent with our observations of Δt_{IR}-independent electron dynamics. On the other hand, in pyridine-capped NCs, the e−h coupling is strong immediately after photoexcitation (holes are inside the NC), but is significantly reduced after the hole transfer to the pyridine, which explains the more than 10-

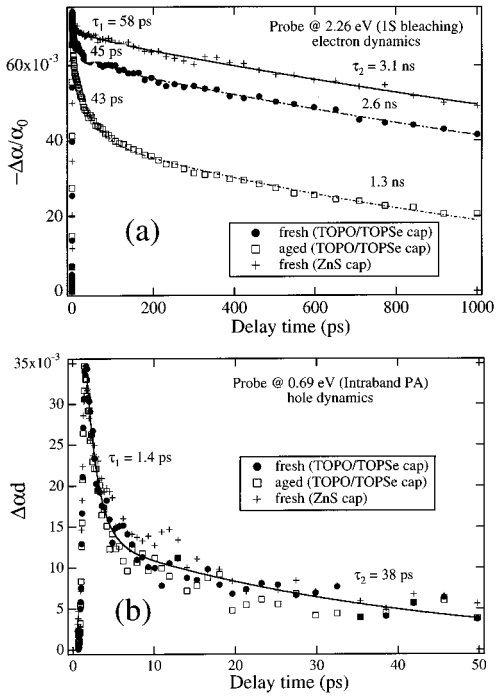

Figure 10. (a) Dynamics of the 1S bleaching at 2.26 eV (a) and hole-intraband absorption at 0.69 eV (b) in 1.7 nm CdSe NCs with differently prepared surfaces: fresh (circles) and aged (squares) TOPO/TOPSe-capped NCs, and NCs overcoated with a ZnS layer (crosses). Lines are fits to a double-exponential decay.

fold slowing down in the electron intraband relaxation (Figure 9a). However, even in the charge-separated system, the electron relaxes back to the ground state on a ps time scale which is much faster than expected for phonon-dominated relaxation. This indicates that even in the case of a significant spatial separation between an electron and a hole, Coulomb e−h interactions can be strong enough to provide an efficient channel for electron energy losses. This can be rationalized as arising from the fact that the Coulomb coupling does not require a direct overlap between electron and hole wave functions and scales relatively slowly (inversely) with the e−h separation.

5. Depopulation Dynamics of Nanocrystal Quantized States

5.1. Electron and Hole Relaxation Paths in Nanocrystals. Intraband relaxation leads to a fast establishment of quasi-equilibrium populations of electron and hole NC quantized states. Depopulation of these states occurs via a variety of radiative and nonradiative mechanisms. The most important processes competing with radiative recombination are carrier trapping at surface/interface states and Auger recombination. At low pump intensities (less than one e−h pair per NC on average), the role of Auger effects is negligible and nonradiative relaxation is primarily due to carrier trapping.[38,50]

Since 1S bleaching signals are dominated by occupations of the lowest 1S electron state, the 1S $\Delta\alpha$ decay can be used to evaluate the rate of electron-trapping processes. In CdSe NCs, the 1S bleaching decay shows two distinct regions. It starts with a relatively fast sub-100 ps relaxation, which is followed by a slower nanosecond decay (Figure 10a). The amplitude of the fast component is sensitive to the degree of surface passivation, as obvious from comparison of the 1S bleaching dynamics in freshly prepared and aged TOPO/TOPSe-passivated NCs (circles and squares in Figure 10a, respectively), and NCs overcoated with a ZnS layer (crosses in Figure 10a). As indicated by PL quantum yield measurements, the quality of the "electronic" passivation of surface traps is progressively increased in going from the aged to the fresh TOPO/TOPSe-capped sample, and then to the sample overcoated with ZnS. The improvement in surface passivation leads to the suppression of the fast decay component, indicating that it is due to trapping at surface defects. Furthermore, the correlations between the loss of the TOPO/TOPSe passivation (these molecules are coordinated to surface metal ions)[7,9] and the enhancement of the fast component indicate that the electron traps are likely associated with metal dangling bonds.

Because interband TA signals in NCs are dominated by electron populations, it is difficult to extract from them hole dynamics. Separation of electron and hole signals is possible using intraband TA spectroscopy, with an IR probe tuned in resonance with either electron or hole intraband transitions.[38,57] In the near-IR range from 0.4 to 1 eV, inraband TA of CdSe NCs can be decomposed into two components: due to electron and hole intraband absorptions.[38,50] In contrast to the initial electron dynamics, which can be controlled by surface passivation, the initial hole relaxation is practically unaffected by NC surface properties, as clearly seen from comparison of dynamics of the hole intraband signals recorded for samples with three different surface passivations (Figure 10b; shown are the data for the same set of samples as in panel a). All three samples show a nearly identical 1.4 ps decay, indicating fast hole relaxation, independent of NC surface properties. The fast decay of hole near-IR intraband signals (0.5−2 ps time constants) is seen in all TOPO/TOPSe- and ZnS-capped CdSe NCs with sizes from 1 to 4 nm.[38,50] The fact that hole dynamics are extremely fast in all types of samples, including NCs overcoated with a ZnS layer, indicates that these dynamics are not due to trapping at localized surface defects such as a vacancy, but rather due to relaxation into intrinsic NC states. The exact nature of the ultrafast decay of the hole intraband absorption is not clear. It can be, for example, due to relaxation within the fine structure of levels corresponding to the band-edge exciton states with different oscillator strengths,[32,58] or due to relaxation into "intrinsically" unpassivated interface or self-trapped[59] surface states optically decoupled from (or only weakly coupled to) the initially excited valence-band states.

5.2. Quantum-Confined Auger Recombination. In the regime of muiltiple e−h pair excitation, depopulation of NC quantized states can occur via Auger recombination. Auger recombination is a nonradiative multiparticle process, leading to the recombination of e−h pairs via energy transfer to a third particle (an electron or a hole) which is re-excited to a higher energy state.[60,61] In NCs, confinement-induced enhancement in Coulomb interactions and relaxation in the translation momentum conservation should lead to increased Auger rates in comparison with those in bulk materials,[62] whereas the atomic-like structure of energy levels in NCs should hinder Auger processes because of the reduced availability of final states satisfying energy conservation. As a result, Auger recombination can only occur efficiently with the participation of a phonon (as a four-particle process) or with the involvement of a final state from the continuum of states outside the NC (Auger ionization).[62,63] The complex interplay between the above effects complicates a theoretical analysis of quantum-confined Auger recombination and highlights the need for experimental mapping of the size-dependent Auger rates.

Experimental data for the Auger effect in NCs have typically been analyzed within a bulk semiconductor approach by introducing an effective carrier concentration in the NC (n_{eh} =

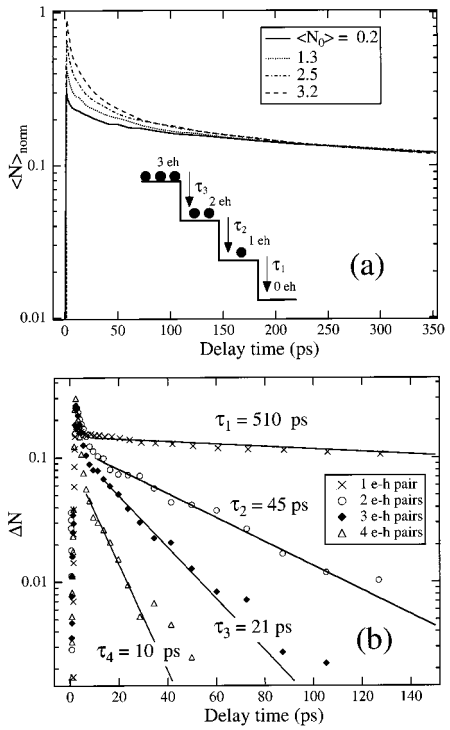

Figure 11. (a) Pump-dependent dynamics of NC average populations in the 2.3 nm sample normalized to match their long-term decay values Inset: Quantized steps in quantum-confined Auger recombination in NCs. (b) Dynamics of the 1-, 2-, 3-, and 4-e−h pair states (symbols) extracted from the TA data for the 2.3 nm sample (see text), fit to a single-exponential decay (solid lines).

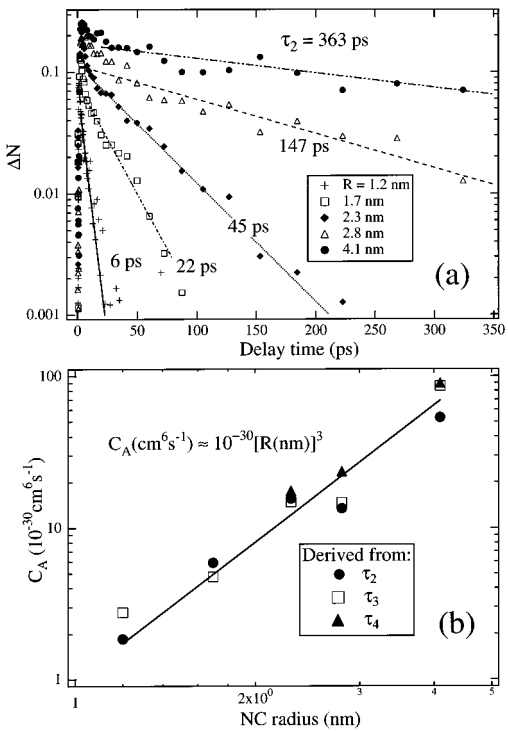

Figure 12. (a) 2-e−h pair dynamics in NCs with radii 1.2, 1.7, 2.3, 2.8, and 4.1 nm (symbols), fit to a single-exponential decay (lines). (b) Size dependence of the Auger constant (symbols), fit to the dependence $C_A \propto R^3$ (line); circles, squares, and triangles correspond to data derived from the lifetimes of the 2-, 3-, and 4-pair states, respectively.

N/V_0) and a cubic carrier decay rate ($C_A n_{eh}^3$, where C_A is the Auger constant).[20,64] However, it is not obvious that this approach should be valid in the regime of a few e−h pairs per NC, for which recombination occurs as a sequence of quantized steps from the N to $N-1$, $N-2$, ...and finally to the 1 e−h pair state (inset to Figure 11a). In the "quantized" regime, Auger recombination is characterized not by a continuum of density-dependent recombination times $\tau_A = (C_A n_{eh}^2)^{-1}$ as in bulk materials, but by a set of discrete recombination constants, characteristic of the decay of the 2−, 3−, ..., e−h pair NC states.

To study multiparticle decay in NCs, we monitored relaxation of the 1S bleaching using a pump−probe experiment (see section 3.2). The dynamics of carrier population were derived from the measured $\Delta\alpha(t)$ signals using the "universal" relationship between $\Delta\alpha/\alpha_0$ and $\langle N\rangle$ given by eq 6 (section 3.3). In Figure 11a, we show the normalized NC population dynamics for a 2.3 nm sample measured at carrier injection levels $\langle N_0\rangle$ from 0.2 to 3.2. Over this range of excitation densities, the temporal evolution of $\langle N\rangle$ is dominated by contributions from NCs in 4-, 3-, 2-, and 1-e−h pair states: $\langle N(t)\rangle \approx [4n_4(t) + 3n_3(t) + 2n_2(t) + n_1(t)]/n_0$, where n_0 is the total density of NCs in the sample, and n_N ($N = 1-4$) is the concentration of NCs having N e−h pairs. The NC multiparticle dynamics can be described by the set of coupled rate equations,[21] with a straightforward solution given by a sum of exponential terms: $\langle N(t)\rangle = \sum_{N=1}^{4} A_N e^{-t/\tau_N}$, where A_N are time-independent coefficients determined by initial injection densities and τ_N is the lifetime of the N-pair NC state.

We developed a simple subtractive procedure to extract single-exponential dynamics that are characteristic of the decay of different multiple-pair NC states from the measured $\langle N(t)\rangle$ time transients. In this procedure, the time transients are normalized so that the long-time decay values match (Figure 11a), which is possible due to the fact that at long times after photoexcitation, the decay is governed by singly-excited NCs, independent of the initial carrier density. We subtract the low-pump intensity trace ($\langle N_0\rangle < 1$; single e−h pair decay) from traces recorded at $\langle N_0\rangle > 1$, which yields dynamics $\Delta N(t)$ due to relaxation of multiple-pair states with $N \geq 2$. For initial carrier densities $1 < \langle N_0\rangle < 2$, this procedure yields the two-pair state dynamics (circles in Figure 11b), with a faster initial component due to contribution from states with a larger number of excited pairs. The two-pair decay is further subtracted (after normalization) from the $\Delta N(t)$ time transients detected at $\langle N_0\rangle > 2$ to derive dynamics of states with $N \geq 3$. This procedure can be repeated to extract dynamics of NC states with $N = 4$, 5, etc.

The extracted dynamics of the 2-, 3- , and 4-pair states (Figure 11b) indicate that the carrier decay becomes progressively faster with increasing the number of e−h pairs per NC, as expected for Auger recombination. In bulk semiconductor arguments, the effective decay time constant τ_N in the Auger regime is given by $\tau_N^{-1} = C_A(N/V_0)^2$ ($N \geq 2$). This expression predicts a ratio $\tau_4:\tau_3:\tau_2 = 0.25:0.44:1$ which is very close to the ratio 0.22:0.47:1 of experimentally-determined times of 4-, 3-, and 2-pair relaxation (10, 21, and 45 ps, respectively). The quantitative match of scaling for the multiparticle relaxation times indicates that the decay rates for quantum-confined Auger recombination are cubic with respect to the carrier density ($dn_{eh}/dt \propto -n_{eh}^3$), just as in bulk materials.

TA data for NCs of different sizes (Figure 12a) indicate that the τ_2 time constant rapidly decreases with decreasing NC size following a cubic size dependence ($\tau_2 \propto R^3$);[21] $\tau_2 = 363$ ps in NCs with $R = 4.1$, and reduces down to 6 ps for NCs with $R = 1.2$ nm. Interestingly, the time constants measured for the 3- and 4-pair decay follows the same size dependence as that of the 2-pair state, such that the time-constant ratios predicted by

the bulk-semiconductor model holds for all NC sizes.[21] Simple bulk-material reasoning would suggest that the enhancement in the Auger decay in smaller particles is caused by an effective increase in carrier concentrations resulting from the increased spatial confinement. However, the R^3 size dependence of relaxation times measured experimentally is different from the R^6 dependence predicted by the bulk-semiconductor model, which shows that in 3D-confined systems the Auger "constant" depends on the particle size. The Auger constant derived from the relaxation data decreases with reducing NC radius as R^3 from $\sim 7 \times 10^{-29}$ cm^6 s^{-1} for $R = 4.1$ nm to $\sim 2 \times 10^{-30}$ cm^6 s^{-1} for $R = 1.2$ nm (Figure 12b). For all NC sizes, the C_A values calculated by using lifetimes of 2-, 3-, and 4-e−h pair states are close to each other (compare data shown by circles, squares and triangles in Figure 12b), indicating that the cubic density dependence of the Auger rates holds for all sizes between 1 and 4 nm.

We used colloidal samples with two types of surface passivations (TOPO/TOPSe and ZnS) and in two different matrices (hexane or a transparent polymer) to study the effect of NC surface/interface properties on Auger rates. As demonstrated in section 5.1, surface modification has a significant effect on single-electron dynamics. However, high-pump intensity TA data indicate that multiparticle dynamics (e.g., the 2-e−h pair decay) are not significantly affected by surface/interface properties.[21] This strongly suggests that Auger recombination in the samples studied is dominated by processes involving NC "volume" states, without a significant contribution from the Auger ionization.

6. Conclusions

We have reviewed data on ultrafast carrier dynamics and resonant optical nonlinearities in CdSe colloidal NCs. Analysis of band-edge TA allowed us to establish an accurate relationship between the magnitude of TA signals and NC average populations. This relationship was particularly useful in studies of multiparticle Auger recombination, in which we were able to quantify relaxation rates of multiple e−h pair states and to derive the dependence of these rates on NC sizes. Studies of intraband carrier dynamics established well-defined time scales for electron intraband relaxation. These studies also provided strong evidence that this relaxation occurs neither by phonon emission nor by coupling to defects, but by e−h energy transfer mediated by the intrinsic Auger-type interactions. We clearly observed correlations between NC surface properties and depopulation dynamics of electron quantized states at the stage following intraband relaxation. Relaxation data for NCs with differently treated surfaces indicated that the depopulation of the lowest 1S electron level is directly affected by trapping at surface defects. On the other hand, the hole relaxation pathways remain more poorly understood. We observed extremely fast depopulation of the initially excited valence-band states, with dynamics that are not significantly influenced by NC surface treatment. This suggests a relaxation mechanism that is not due to trapping at localized surface defects, but rather involves NC intrinsic states. The exact nature of these states remains unclear, due partially to an incomplete knowledge of valence band energy structures and the structure of the surface/interface states. Presently, a relatively poor understanding of hole relaxation pathways does not allow us to correlate the data on ultrafast carrier dynamics with the measured PL efficiencies of NC samples. Studies of time-resolved femtosecond PL, started recently in our laboratory, will help in establishing this important correlation. Significant progress in understanding ultrafast carrier dynamics would be achieved by developing capabilities for single NC femtosecond spectroscopy. This work is also proceeding in our laboratory. Further, we will pursue studies of carrier dynamics in systems of communicating NCs (such as in quantum dot solids)[14,15] and NCs interacting with organic environments (such as in NC/polymer blends).[13] This work is an important step toward incorporating NCs into optical, electronic, and optoelectronic devices.

Acknowledgment. This review represents a brief summary of the recent research of the Los Alamos femtosecond group in the field of colloidal quantum dots. I would like to thank the current and past members of the group for contributing to this work. I gratefully acknowledge the contributions of D. McBranch, A. Mikhailovsky, S. Xu, C. Schwarz, A. Malko, and J. Hollingsworth. This work would be impossible without excellent samples provided by C. Leatherdale and M. Bawendi. Also, I would like to thank Al. Efros and M. Bawendi for numerous discussions of photophysics of quantum dots. This work was supported by Los Alamos Directed Research and Development Funds, under the auspices of the U. S. Department of Energy.

References and Notes

(1) Efros, Al. L.; Efros, A. *Sov. Phys. Sem.* **1982**, *16*, 772.
(2) Brus, L. *J. Chem. Phys.* **1983**, *79*, 5566.
(3) Brus, L. *Appl. Phys. A* **1991**, *53*, 465.
(4) Alivisatos, A. *Science* **1996**, *271*, 933.
(5) Ekimov, A. *J. Lumin.* **1996**, *70*, 1.
(6) Borrelli, N.; Hall, D.; Holland, H.; Smith, D. *J. Appl. Phys.* **1987**, *61*, 5399.
(7) Murray, C.; Norris, D.; Bawendi, M. *J. Am. Chem. Soc.* **1993**, *115*, 8706.
(8) Majetich, S.; Carter, A. *J. Phys. Chem.* **1993**, *97*, 8727.
(9) Kuno, M.; Lee, J. K.; Dabbousi, B. O.; Miulec, F. V.; Bawendi, M. G. *J. Phys. Chem.* **1993**, *97*, 9869.
(10) Kortan, A.; Hull, R.; Opila, R.; Bawendi, M.; Steigerwald, M.; Carroll, P.; Brus, L. E. *J. Am. Chem. Soc.* **1990**, *112*, 1327.
(11) Hines, M.; Guyot-Sionnest, P. *J. Phys. Chem.* **1996**, *100*, 468.
(12) Counio, G.; Esnouf, S.; Gacoin, T.; Boilot, J. *J. Phys. Chem.* **1996**, *100*, 20021.
(13) Greenham, N.; Peng, X.; Alivisatos, A. *Phys. Rev. B* **1996**, *54*, 17628.
(14) Murray, C.; Kagan, C.; Bawendi, M. *Science* **1995**, *270*, 1335.
(15) Mićić, O.; Jones, K.; Cahill, A.; Nozik, A. *J. Phys. Chem. B* **1998**, *102*, 9791.
(16) Benisty, H.; Sotomayor-Torres, C.; Weisbuch, C. *Phys. Rev. B* **1991**, *44*, 10945.
(17) Woggon, U.; Giessen, H.; Gindele, F.; Wind, O.; Fluegel, B.; Peyghambarian, N. *Phys. Rev. B* **1996**, *54*, 17681.
(18) Klimov, V. I.; McBranch, D. W. *Phys. Rev. Lett.* **1998**, *80*, 4028.
(19) Nuss, M. C.; Zinth, W.; Kaiser, W. *Appl. Phys. Lett* **1986**, *49*, 1717.
(20) Ghanassi, M.; Schanne-Klein, M.; Hache, F.; Ekimov, A.; Ricard, D. *Appl. Phys. Lett.* **1993**, *62*, 78.
(21) Klimov, V. I.; Mikhailovsky, A. A.; McBranch, D. W.; Leatherdale, C. A.; Bawendi, M. G. *Science* **2000**, *287*, 1011.
(22) Klimov, V. In *Handbook on Nanostructured Materials and Nanotechnology*; Nalwa, H., Ed.; Academic Press: San Diego, CA, 1999; Volume 4, p 451.
(23) Norris, D.; Sacra, A.; Murray, C.; Bawendi, M. *Phys. Rev. Lett.* **1994**, *72*, 2612.
(24) Logunov, S.; Green, T. C.; Marquet, S.; El-Sayed, M. A. *J. Phys. Chem. A* **1998**, *102*, 5658.
(25) Guyot-Sionnest, P.; Shim, M.; Matranga, C.; Hines, M. *Phys. Rev. B* **1999**, *60*, 2181.
(26) Norris, D.; Bawendi, M. *Phys. Rev. B* **1996**, *53*, 16338.
(27) Ekimov, A. I.; Hache, F.; Schanne-Klein, M. C.; Ricard, D.; Flytzanis, C.; Kudryavtsev, I. A.; Yazeva, T. V.; Rodina, A. V.; Efros, Al. L. *J. Opt. Soc. Am. B* **1993**, *10*, 100.
(28) Xia, J.-B. *Phys. Rev. B* **1989**, *40*, 8500.
(29) Efros, Al. L. *Phys. Rev. B* **1992**, *46*, 7448.
(30) Efros, Al. L.; Rodina, A. *Phys. Rev. B* **1993**, *47*, 10005.
(31) Takagahara, T. *Phys Rev. B* **1993**, *47*, 4569.
(32) Nirmal, M.; Norris, D.; Kuno, M.; Bawendi, M.; Efros, Al. L.; Rosen, M. *Phys Rev. Lett.* **1995**, *75*, 3728.
(33) Ninomiya, S.; Adachi, A. *J. Appl. Phys.* **1995**, *78*, 4681.

(34) Ricard, D.; Ghanassi, M.; Schanneklein, M. *Opt. Commun.* **1994**, *108*, 311.
(35) Shah, J. *Ultrafast Spectroscopy of Semiconductors and Semiconductor Nanostructures*; Springer: Berlin, 1999.
(36) Hunsche, S.; Dekorsy, T.; Klimov, V.; Kurz, H. *Appl. Phys. B* **1996**, *62*, 3.
(37) Klimov, V.; Haring Bolivar, P.; Kurz, H. *Phys. Rev. B* **1996**, *53*, 1463.
(38) Klimov, V. I.; Schwarz, C. J.; McBranch, D. W.; Leatherdale, C. A.; Bawendi, M. G. *Phys. Rev. B* **1999**, *60*, R2177.
(39) Klimov, V.; Hunsche, S.; Kurz, H. *Phys. Rev. B* **1994**, *50*, 8110.
(40) Hu, Y.; Koch, S.; Linberg, M.; Peyghambarian, N.; Pollock, E.; Abraham, F. *Phys. Rev. Lett.* **1990**, *64*, 1805.
(41) Kang, K.; Kepner, A.; Gaponenko, S.; Koch, S.; Hu, Y.; Peyghambarian, N. *Phys. Rev. B* **1993**, *48*, 15449.
(42) Pantke, K. H.; Erland, J.; Hvam, J. M. *J. Crystal Growth* **1992**, *117*, 763.
(43) Klimov, V. I.; McBranch, D. W. *Opt. Lett.* **1998**, *23*, 277.
(44) Fork, R.; Shank, C. V.; Hirlimann, C.; Yen, R. *Opt. Lett.* **1983**, *8*, 1.
(45) Conwell, E. *High Field Transport in Semiconductors*; Academic Press: New York, 1967.
(46) Prabhu, S.; Vengurlekar, A.; Shah, J. *Phys. Rev. B* **1995**, *51*, 14233.
(47) Klimov, V.; Haring Bolivar, P.; Kurz, H. *Phys. Rev. B* **1995**, *52*, 4728.
(48) Bockelmann, U.; Bastard, G. *Phys. Rev. B* **1990**, *42*, 8947.
(49) Shum, K.; Wang, W. B.; Alfano, R.; Jones, K. *Phys. Rev. Lett.* **1992**, *68*, 3904.
(50) Klimov, V. I.; McBranch, D. W.; Leatherdale, C. A.; Bawendi, M. G. *Phys. Rev. B* **1999**, *60*, 13740.
(51) Inoshita, T.; Sakaki, H. *Phys. Rev. B* **1992**, *46*, 7260.
(52) Sercel, P. *Phys. Rev. B* **1995**, *51*, 14532.
(53) Bockelmann, U.; Egler, T. *Phys. Rev. B* **1992**, *46*, 15574.
(54) Efros, Al. L.; Kharchenko, V. A.; Rosen, M. *Solid State Commun.* **1995**, *93*, 281.
(55) Klimov, V. I.; Mikhailovsky, A. A.; McBranch, D. W.; Leatherdale, C. A.; Bawendi, M. G. *Phys. Rev. B* **2000**, *61*, R13349.
(56) Burda, C.; Green, T. C.; Link, S.; El-Sayed, M. A. *J. Phys. Chem. B* **1999**, *103*, 1783.
(57) Guyot-Sionnest, P.; Hines, M. *Appl. Phys. Lett.* **1998**, *72*, 686.
(58) Efros, A. L.; Rosen, M.; Kuno, M.; Nirmal, M.; Norris, D.; Bawendi, M. *Phys Rev. B* **1996**, *54*, 4843.
(59) Banyai, L.; Gilliot, P.; Hu, Y.; Koch, S. *Phys. Rev. B* **1992**, *45*, 14136.
(60) Chatterji, D. *The Theory of Auger Transitions*; Academic Press: London, 1976.
(61) Landsberg, P. *Recombination in Semiconductors*; University Press: Cambridge, UK, 1991.
(62) Chepic, D.; Efros, Al. L.; Ekimov, A.; Ivanov, M.; Kharchenko, V. A.; Kudriavtsev, I. *J. Lumin.* **1990**, *47*, 113.
(63) Efros Al. L.; Rosen, M. *Phys. Rev. Lett.* **1997**, *78*, 1110.
(64) Klimov, V. I.; McBranch, D. W. *Phys. Rev. B* **1997**, *55*, 13173.